

Unravelling emergence of chirality in click-chemistry polymers down to the single-chain level

Received: 25 September 2024

Accepted: 4 July 2025

Published online: 22 July 2025

Xuecong Li^{1,2}, Sidharam P. Pujari¹, Jasper van der Gucht²,
Han Zuilhof^{1,3}✉ & Francesco Simone Ruggeri^{1,2}✉

Chirality plays a critical role in the structure and function of natural and synthetic polymers, impacting their mechanical, optical, and electronic properties. However, a comprehensive understanding of the hierarchical emergence of chirality from monomers to macromolecular assemblies remains elusive, largely because of current limitations in studying their chemical-structural properties at the nanoscale. Here, we unravel the emergence of different forms of chirality from small molecules to their resulting polymers and supramolecular assemblies. We leverage bulk spectroscopic methods combined with the development of acoustical-mechanical suppressed infrared nanospectroscopy, to empower chemical-structural analysis of single-polymer chains. This ultra-high sensitivity allows identifying key functional groups as a signature for different forms of chirality: CH groups for central chirality in small molecules; C=O groups for backbone and supramolecular chirality in heterogeneous polymers. This work opens a new single-molecule chemical angle of observation into chirality and (bio)-polymers for the rational design in material science, biotechnology, and medicine.

Chirality plays crucial roles in the structure and functionalities of biomacromolecules and synthetic polymers^{1,2}. Nucleic acids, proteins, natural carbohydrates, and several other naturally occurring polymers are composed of chiral building blocks contributing to their unique 3D structure and function, including biological recognition³, transcription⁴, and enzymatic processes⁵. Taking inspiration from nature, polymer scientists have designed innovative materials where specific arrangement of chiral centres allows unique mechanical⁶, optical⁷, and electronic⁸ properties. However, understanding how to tune the molecular and chiral properties of polymers, to achieve new functionalities at the macromolecular level in advanced materials, remains a key challenge⁹.

A critical yet unresolved question is how chirality hierarchically emerges from the sub-molecular to the macromolecular level¹. Previous work has studied the influence of molecular central chirality and

polymerization conditions on polymer backbone chirality^{10–12}. However, the mechanisms linking the stereochemistry of the small monomeric building blocks (central chirality), the arrangement and conformation of the polymer backbone (helical chirality), and the organization of single polymer chains in assemblies (supramolecular chirality) are still unclear¹³. This knowledge gap arises from the limits of current state-of-the-art analytical methods to characterize the complex manifestation of chirality in polymer systems across multiple length scales.

Bulk circular dichroism (CD)¹⁴, infrared (IR) spectroscopy¹⁵, and vibrational circular dichroism¹⁶ can provide insights into the chirality of molecular systems. However, bulk methods cannot obtain single-molecule level information on heterogeneous systems; thus, they are not able to differentiate the diverse manifestations of chirality at the (sub)-molecular (central), backbone (helical), and assemblies

¹Laboratory of Organic Chemistry, Wageningen University, Wageningen, the Netherlands. ²Physical Chemistry and Soft Matter, Wageningen University, Wageningen, the Netherlands. ³School of Pharmaceutical Science and Technology, Tianjin University, Tianjin, China. ✉e-mail: han.zuilhof@wur.nl; simone.ruggeri@wur.nl

(supramolecular) level^{17–19}. Nano-imaging methods allow visualizing polymeric structures down to the single-chain level and excel in detailing their molecular and chiral conformations. Cryogenic electron microscopy (cryo-EM)²⁰ collects 2D images of single helical molecules with <0.5 nm resolution, although it is limited by the need for extensive sampling and computational 3D model reconstruction²¹, and has difficulties in reconstructing the structure of molecules with less-defined helices²⁰. Atomic Force Microscopy (AFM)²² can image the 3-D morphology of single polymers chains and their assemblies with angstroms resolution in the Z direction, and <1 nm resolution on the 2-D plane²³. However, both cryo-EM and AFM fall short in discerning chemical information, thereby limiting the understanding of backbone and supramolecular chirality emergence as a function of the central chirality of monomers¹⁸.

To unravel polymer properties, the chemical power of bulk spectroscopy and single-molecule imaging of AFM has been combined in nano-chemical imaging and spectroscopic techniques. Tip-enhanced Raman spectroscopy²⁴ and scattering scanning near-field optical microscopy allowed chemical imaging of single small organic molecules²⁵, 2D monolayers²⁶, or larger polymer systems²⁷. However, because of scattering, plasmonic, and tip-reproducibility effects causing spectral deformation or band suppression, they are limited in extracting structural data from (bio-)organic polymers^{28,29}. As a key advantage compared to scattering methods, AFM-based photothermal infrared nanospectroscopy (AFM-IR) has proven to acquire robust and reproducible nano-chemical and structural information from (bio-)organic polymers¹⁹. AFM-IR is free from scattering effects and independent of the surface/probe geometry³⁰. While we have demonstrated to achieve AFM-IR single-molecule sensitivity, the method has up to now been limited to large biomolecules (>400 kDa), while requiring the enhancement of its signal at a gold probe/surface nanogap³¹. These technological and sensitivity constraints have precluded nanospectroscopic investigations of single polymer chains of smaller molecular weights and on different surfaces necessary to preserve their molecular conformations³¹, thus restricting polymer analysis primarily to mesoscopic and sub-micrometre scales on relatively homogenous model systems, such as monolayers³², block copolymers³³ and polymer blends^{30,34}.

Here, we gain molecular insights into the hierarchical emergence of chirality from single monomers (central) to polymers (backbone/helical) and their assemblies (supramolecular). To reach this objective, we designed a system with monomers and polymers possessing the same connectivity, but different chirality. We use racemic and chiral monomers to produce both racemic and homochiral (>99% ee) polymers of ~200 kDa, and their supramolecular assemblies, via enantiospecific click reactions³⁵. We use a multiscale, correlative approach to identify and unravel the relationship among different forms of chirality (central, backbone, supramolecular), from bulk (CD, IR, UV-Vis) to single-chain and supramolecular assemblies imaging (AFM). To uncover the correlation between our bulk and single-molecule imaging observations, we then push the limits of AFM-IR nano-chemical analysis. We reach ultra-high sensitivity down to the single-chain level on non-metallic surfaces, revealing the chemical-structural origin of the emergence of supramolecular chirality. Our work paves the way to generalise the characterisation of the mechanisms governing the emergence of chirality in (bio-)polymers, which is key for the rational design of innovative functional chiral macromolecules in healthcare and materials science.

Results

Multiscale analysis of origin and emergence of chirality

Figure 1 illustrates our framework to perform a multiscale analysis of the emergence of chirality. While stereogenic centres in molecules define chirality, this term alone is insufficient to differentiate the different forms of chirality that emerge in polymeric systems over

multiple length scales. We designed a same connectivity, different chirality system to unravel this hierarchical emergence (Fig. 1a): (i) from central chirality in small monomeric molecules; (ii) to backbone chirality in single polymer chains, defined as the geometric configuration of the main axis of symmetry of the polymer induced by helical chirality; (iii) and supramolecular order in their assemblies. We selected as a model system chiral sulfur fluoride exchange (SuFEx) polymers, a novel class of environmentally friendly and sustainable polymers produced via click chemistry^{35,36}.

To investigate how chirality manifests from the central chirality of molecules to the backbone and supramolecular chirality of polymers, we implemented a multimodal and multiscale approach (Fig. 1b–e). We leveraged bulk Chiral High-Performance Liquid Chromatography (Chiral-HPLC), CD, IR, and ultraviolet-visible (UV-Vis) spectroscopies (Fig. 1b, c) to evaluate and compare the average chemical-structural properties of racemic and chiral monomers and polymers. AFM and AFM-IR empowered us to gain a single-molecule understanding of polymer morphology and chemical properties. Phase-controlled AFM nano-imaging allowed visualizing directly backbone helical chirality at the single-chain level, and unravelling heterogeneity among individual polymer chains and their supramolecular self-assemblies (Fig. 1d)^{37,38}. The development of acoustical-mechanical suppressed AFM-IR enabled the correlation of the morphological information with the corresponding molecular and chemical-structural properties of single-chains assemblies (Fig. 1e).

The chiral building blocks, their synthesis and characterisation

Our framework with the same connectivity but different chirality (Fig. 1a) included monomers, linkers, repeating units, and polymers (Fig. 2a–c, Supplementary Fig. 1)^{18,35}.

We synthesised two small molecules serving as building blocks of the polymers: a chiral molecule and a linker (Fig. 2a, Supplementary Fig. 1, Methods). The chiral di(sulfonimidoyl fluoride) molecule (*di-SF*) had two chiral centres having *R* (red) or *S* (blue) configuration (Fig. 2a). Molecules with mixed configurations were termed *rac*-monomers. Enantiopure chiral *di-SFs* molecules were termed χ -monomers. The linker is a symmetric bis(phenyl ether) (*di-phenol*) molecule, which is non-chiral and acted as linker for the polymerization (Fig. 2a, link-monomer). The monomers and link-monomer were repetitively bonded via the SuFEx reaction to form the polymers (Fig. 2b, Supplementary Fig. 1, Methods). *Rac*-monomers may lead to non-helical polymers termed here *rac*-polymer, while the χ -monomers may lead to polymers with helical backbone chirality, termed here χ -polymers. Gel Permeation Chromatography (GPC) determined a molecular weight (MW) and polydispersity (PDI) of (Supplementary Fig. 2): χ -polymer, M_n ~ 209 kDa with \bar{D} = 1.79; *rac*-polymer, M_n ~ 220 kDa with \bar{D} = 1.42.

To mimic the smallest χ - or *rac*-repeating unit of the polymers, we also synthesised a molecule consisting of a χ - or *rac*-monomer linked to a *di-phenol* link-monomer with an additional single methyl cap (Fig. 2c, Supplementary Fig. 1, Methods). These repeating units allowed analysing the differences in chirality between monomers and the resulting polymers, focusing on structural differences rather than variations in the composition and presence of specific functional groups.

We finally synthesised both the *RR* and *SS* enantiomers of chiral χ -monomers, χ -repeating units, and χ -polymers; to compare their properties with the racemic (*rac*-) species. Our SuFEx-based polymer system with the same connectivity, different chirality was designed here to enable the precise control of chirality (achieving 99% ee) while maintaining the same connectivity, making it an ideal platform for systematically studying structure-property relationships in chiral materials.

Bulk Identification of Chirality

We first aimed to prove the presence or absence of chirality in our monomers, repeating units and polymers. We applied bulk chiral HPLC

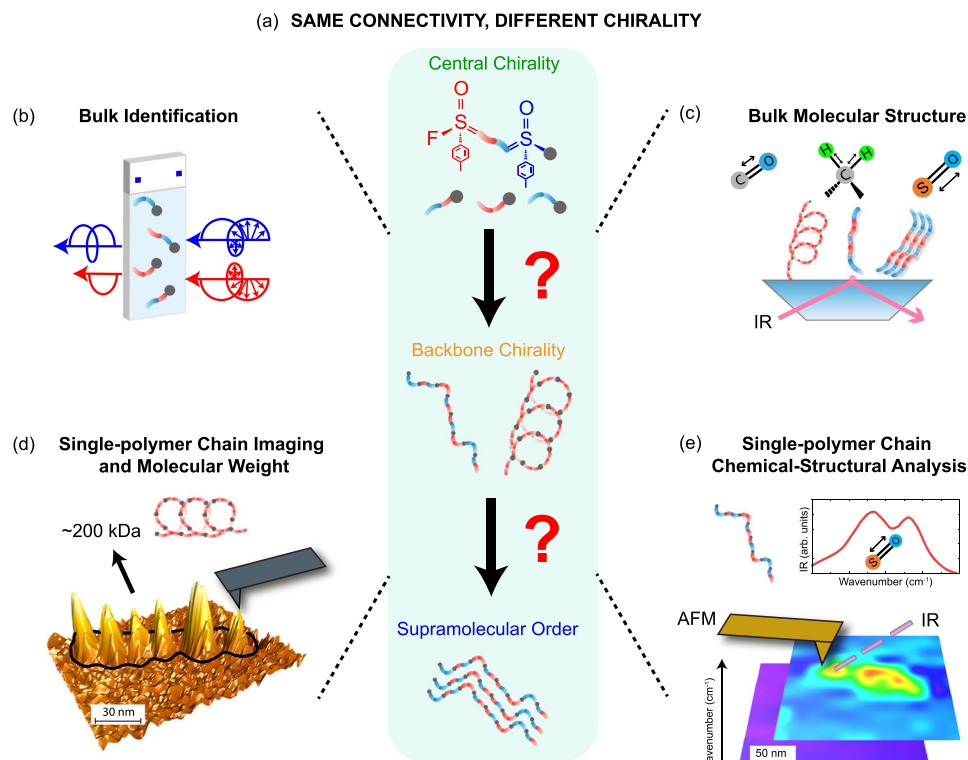


Fig. 1 | Unravel Origin and Emergence of Chirality in Polymers by Multiscale and Multimodal Bulk, Nano-Imaging and Nano-Chemical Analysis. **a** Our designed model system with identical connectivity but varying chiral configurations to study the link between central chirality in monomers, backbone chirality in polymers, and

exploring how variations in chirality result in distinct supramolecular structures. Analysis in bulk with **b** CD, **c** FTIR, and at single molecule level with **d** AFM angstrom-resolution 3D imaging, **e** AFM-IR chemical analysis.

(Supplementary Fig. 3, Supplementary Note 1), CD (Fig. 2, Supplementary Fig. 4, Supplementary Note 2) and Attenuated Total Reflection Fourier Transform Infrared (ATR-FTIR) spectroscopy (Figs. 2–3, Supplementary Fig. 5–7, Supplementary Note 3–4) to investigate the general differences between chiral (χ -) vs racemic (*rac*-) species.

Chiral-HPLC allowed to separate and identify different enantiomers in the monomers and repeating units (Supplementary Fig. 3, Supplementary Note 1). For both monomers and repeating units, we had: (i) *rac*-species with mixed configurations (*RR*, *RS/SR*, *SS*); (ii) enantiomer pure chiral χ -species (*RR*, *SS*). Separation of chiral polymers was hampered by peak broadening due to polymers heterogeneity³⁹.

We further used CD to identify chirality in all χ - versus *rac*- species, including polymers (Fig. 2d–f, Supplementary Fig. 4, Supplementary Note 2)⁴⁰. Racemic molecules and polymers showed flat spectra, proving the absence of chiral asymmetry. Similar behaviour was observed for isolated meso-monomers (100% *RS/SR*, Supplementary Fig. 4). All χ -species (*RR*, *SS*) showed a CD spectrum with two peaks (238 nm, 290 nm), proving chiral asymmetry. Yet, CD did not provide direct information on the configuration of chiral centres; nor it differentiates between central chirality and new sources of chirality, such as backbone chirality emerging during polymer formation⁴¹.

To identify chirality at the molecular level and compare the χ - versus the *rac*- species, we then used ATR-FTIR spectroscopy (Fig. 2g–i, Supplementary Fig. 5–7, Supplementary Note 3–4). Since symmetrical χ -enantiomers (*RR*, *SS*) have the same chemical properties, we focused on the *RR* species. We acquired ATR-FTIR spectra in the mid-IR range of 3200–1000 cm^{-1} . We used chemometrics and Principal Component Analysis (PCA) to evaluate without bias the spectral differences in two spectral regions: 1800–1200 cm^{-1} (Fig. 2g–i, Supplementary Note 4); 3200–2700 cm^{-1} (Supplementary Fig. 5).

The spectra and PCA score plots showed minor differences between *rac*- vs. χ - monomers (Fig. 2g–i, Supplementary Fig. 6,

Supplementary Note 3). Instead, we observed statistically significant differences along the first principal component (PC1) for the *rac*- vs. χ -species of the repeating units (46%) and the polymers (73%). In the 1800–1200 cm^{-1} region, these differences were associated with the: carbonyl group ($\text{C}=\text{O}$, 1780–1620 cm^{-1} , ~50%); carbon-hydrogen groups ($\text{C}-\text{H}$, 1550–1330 cm^{-1} , ~20%); and sulphonyl group ($\text{S}=\text{O}$, 1300–1200 cm^{-1} , ~30%). In the 3200–2700 cm^{-1} region (Supplementary Fig. 6), the differences were associated to the methyl groups (CH_3 , 2925–2800 cm^{-1} , ~60%). Overall, the FTIR analysis suggested that specific molecular bonds ($\text{C}=\text{O}$ and CH_3) could be associated with chirality, with the largest differences observable in polymers.

Bulk structural differentiation of forms of chirality

We leveraged the molecular information contained in the IR spectra to unravel structural differences between χ - versus *rac*-species (Fig. 3). PCA analysis (Fig. 2) allowed to focus on the most significant spectral regions: i) methyl (CH_3) region, 3020–2800 cm^{-1} (Fig. 3a); ii) the carbonyl ($\text{C}=\text{O}$) region, 1780–1620 cm^{-1} (Fig. 3b). Our system with same connectivity but different chirality in turn ensured that the IR spectral differences could be attributed purely to different structural features.

CH_3 groups are abundant and often located directly or closely to chiral centres or the backbone of polymers^{42,43}. Within 3020–2800 cm^{-1} the spectra showed significant differences between *rac*- vs. χ - species (Fig. 3a, c). Monomers showed only minor differences (Supplementary Fig. 5–7). The repeating units instead showed a significantly higher IR absorption of the aromatic CH_3^{as} and CH_3^{s} groups for the *rac*- than the χ -species (Fig. 3c), relative to the aliphatic CH_3^{as} (2970 cm^{-1}) in the link-monomer.

Our system with same connectivity with different chirality allowed to associate the differences in IR absorption of the CH_3 groups for monomers and repeating units purely to their central chirality (Supplementary Note 4)^{8,42,44}. The weaker IR absorption of χ -repeating units

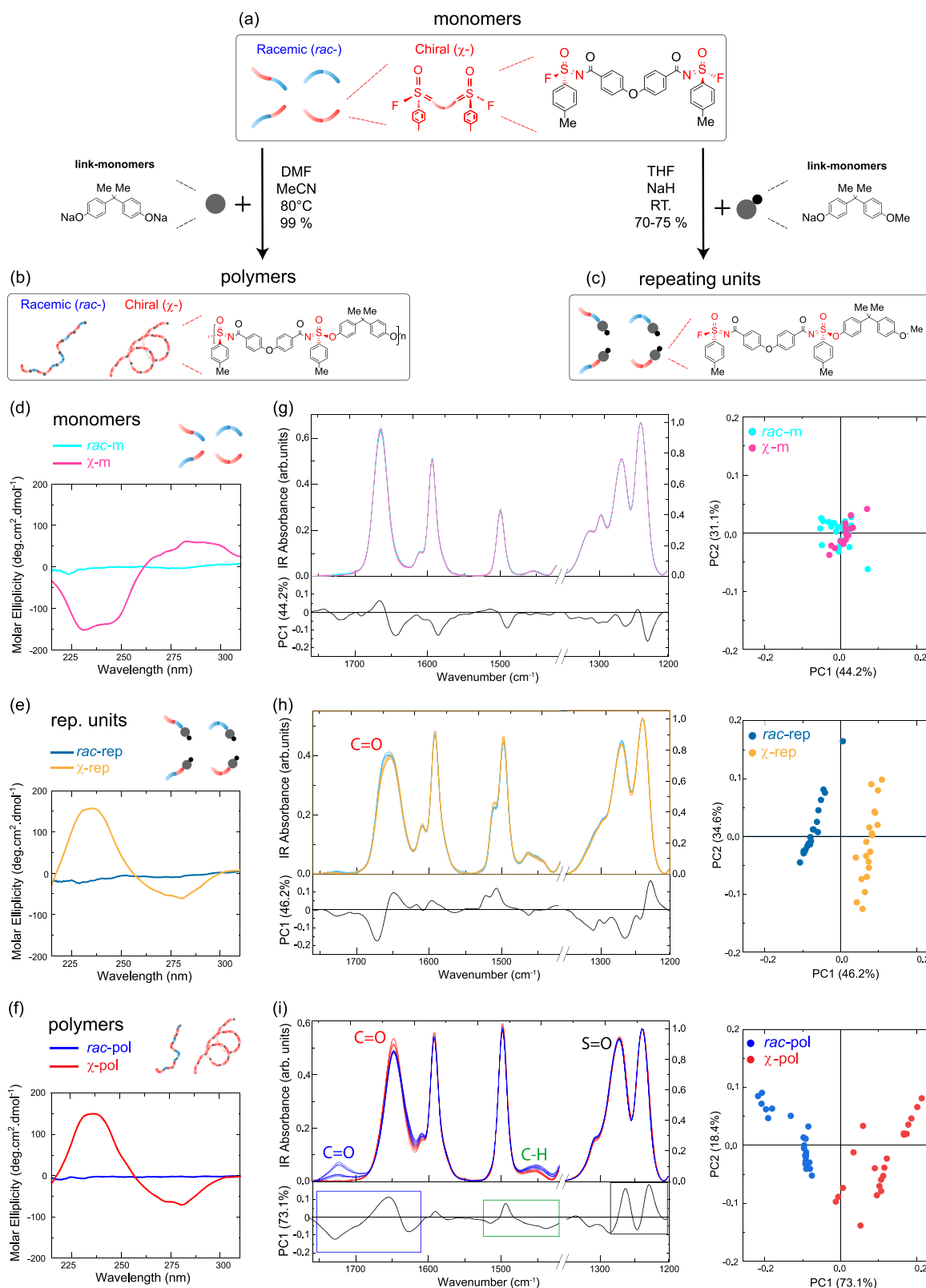


Fig. 2 | Bulk Identification of Chirality of Monomers, Repeating Units and Polymers with Same Connectivity but Different Chirality. Scheme of the SuFEx reaction pathways illustrating the synthesis of **a** racemic (*rac*-) and chiral (χ -) monomers with link-monomers to form **b** *rac*- or χ -polymers; and the **(c)** repeating units, representing the building block of the polymer. **d–f** FCD spectra of monomers, rep. units and polymers. **g–i** Left: IR Spectra and loading plots of PC1 in the range

from 1760–1200 cm⁻¹. For *rac*- and χ - monomers and repeating units: $N = 8$ independent experiments, $n = 40$ spectra each with 512 co-averaging; *rac*- and χ - polymers: $N = 9$ independent experiments, $n = 50$ spectra each with 512 co-averaging. **g–i** Right: PCA score plots analysis of *rac*- and χ - monomers, repeating units, polymers indicate statistically significant differences in the C = O and CH regions (see Fig. 3).

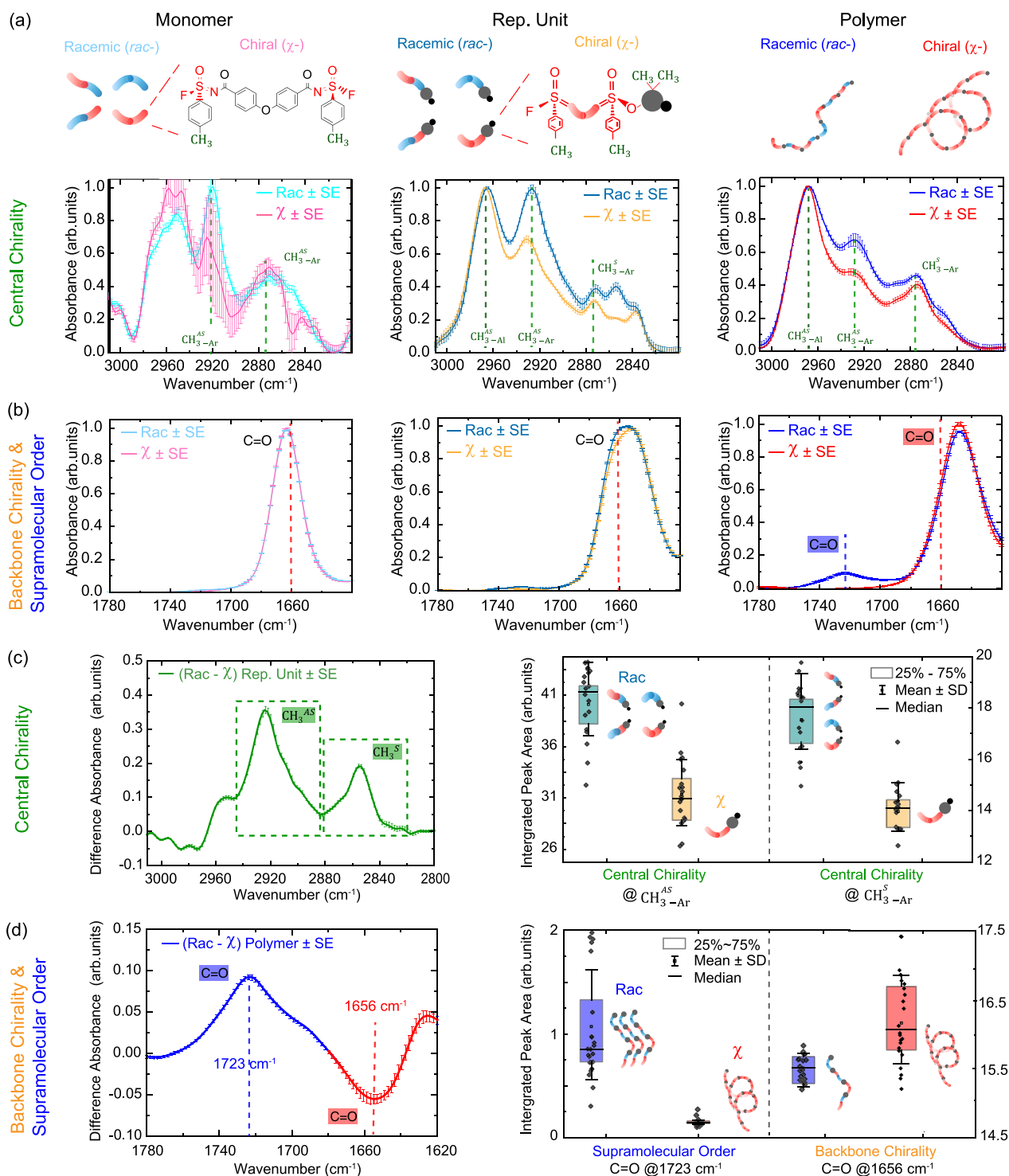


Fig. 3 | Bulk Spectroscopic analysis of molecules and polymers with same connectivity but different chirality. **a** ATR-FTIR spectra of monomer, repeating unit, polymers within CH_3 region (3020–2800 cm^{-1}) sensitive to central chirality. **b** C=O region (1780–1620 cm^{-1}) sensitive to backbone chirality and supramolecular order normalised to their maximum at the S = O peak at 1230 cm^{-1} . $N = 8$ independent experiments, $n = 40$ spectra with 512 co-averaging for monomers and repeating units; $N = 9$ independent experiments, $n = 45$ spectra with 512 co-averaging for polymers; error bars represent SE. **c** Left: Difference spectra for $\text{rac} - \chi$ -repeating units; error bars represent SE. Right: integrated peak areas at 2925 cm^{-1} and 2855 cm^{-1} (rac: green-blue, χ : orange, each data point represents the integration of the peak from a single spectrum), box plot has one SD as whiskers. **d** Left: Difference spectra for $\text{rac} - \chi$ -polymers; error bars represent SE. Right: integrated peak areas at 1723 cm^{-1} and 1656 cm^{-1} (rac: blue, χ : red; each data point represents the integration of the peak from a single spectrum), box plot has one SD as whiskers.

(*RR*) was associated with two less co-planar aromatic CH_3 groups; since these groups are arranged at fixed angles relative to the backbone, leading to reduced planarity because of steric constraints. The increased IR absorption of the *rac*-repeating units may instead be associated with the presence of a larger set of conformations (*RR*, *SS*, *RS/SR*), where the *RS/SR* conformations contribute to a higher IR absorption via a more planar configuration and enhancing electronic delocalization.

Thus, central chirality conformation was associated to an increased planarity of the *rac*-molecules compared to the χ -molecules. The polymers showed also differences in the C-H region, which however may also arise from polymerisation and phenomena such as backbone and supramolecular chirality.

The C=O stretching has been widely related to the structural conformation of the backbone of (bio)-polymers, such as protein^{15,45}. In the range 1700–1620 cm^{-1} , monomers and repeating units did not show significant differences between *rac*- vs. χ -species, while the polymers showed statistically significant differences (Fig. 3b, Supplementary Fig. 7, Supplementary Note 4). Thus, the spectral differences between *rac*- vs. χ -polymers could be ascribed only to other forms of chirality arising from polymerisation and supramolecular assembly. We observed that (Fig. 3b,d): (i) the C=O peak shifted to lower wavenumbers from monomers (1663 cm^{-1}), via the repeating units (1655 cm^{-1}), to polymers (1648 cm^{-1}); (ii) χ -polymers had higher absorption than *rac*-polymers at 1656 cm^{-1} ; (iii) χ -polymers exhibited a single C=O peak, while *rac*-polymers showed the emergence of a second C=O peak at 1723 cm^{-1} .

We associated the shift to lower wavenumbers to electron delocalization caused by the backbone formation in polymers⁴⁶. For the χ -polymers, the increased IR absorption at 1656 cm^{-1} suggested the formation of helices in the backbone during the polymerisation process. Indeed, an IR absorption signature between 1650–1660 cm^{-1} is typically associated with the formation of α -helix structure in protein, where the orientation of a specific sequence of amino acids stabilizes a secondary helical structure⁴⁷ (Fig. 3d, Supplementary Note 4). For the *rac*-polymers, the emergence of the second C=O peak could be associated with (Supplementary Note 4): (i) intramolecular interactions in their *RS/SR* repeating units, via a π - π resonance between the carbonyl groups and phenyl groups, inducing a planar conformation; (ii) enhanced intermolecular π - π stacking of the *RS/SR* phenyls leading to supramolecular assembly and possibly higher chiral order.

To further investigate if emergence of the second C=O peak was associated with intra- or inter-molecular interactions, we conducted UV-Vis spectroscopy measurements on the racemic monomers and polymers as a function of their concentration in solution (Supplementary Fig. 8). The spectra of the polymers revealed a broadening and redshift of absorption peaks with increasing concentration, which are well-established indicators of π - π stacking intermolecular interactions⁴⁸. These modifications were instead absent in the spectra of the monomers. Thus, UV-Vis indicated that *rac*-polymers undergo increased intermolecular π - π interactions rather than intramolecular.

Overall, the IR and UV-Vis structural analysis identified general key molecular vibrations useful to differentiate central chirality in small molecules (CH_3) and backbone/supramolecular chirality in polymers (C=O). The IR absorption of the CH_3 groups highlighted differences in conformation of the molecules associated with their central chirality, resulting in an increased planarity of the racemic molecules. The increased IR absorption of the C=O at 1656 cm^{-1} was associated with the emergence of backbone/helical chirality in the χ -polymers, while the C=O peak splitting and the new IR absorption at 1723 cm^{-1} might indicate increased intermolecular interactions in *rac*-polymers. However, bulk IR and UV-vis prevented studying sample heterogeneity at the single-molecule level to prove: (i) presence of helicity in the backbone for χ -polymers; (ii) supramolecular assembly for the *rac*-

polymers, as suggested by the splitting of the C=O absorption and the emergent peak at 1723 cm^{-1} .

Single-molecule imaging of chirality with Angstrom resolution

To unravel at the single-molecule level the origin of the emergence of chirality from small molecules to polymers, we further leveraged single-molecule 3D imaging. We investigated the presence of backbone helical chirality and the supramolecular assembly state of the *rac*- and χ -polymers with angstrom resolution imaging via phase-controlled AFM (Fig. 4, Supplementary Fig. 9–12, Supplementary Note 5)³⁷.

AFM measurements must be performed on a surface, and performing the measurements on only one substrate could be limiting as it may bias the observed polymer morphology due to the specific surface charge of the substrate. To ensure a more comprehensive analysis, we studied the morphology of the polymers on three atomically-flat substrates with different charge: positive gold, negative mica, and hydrophobic HOPG. On hydrophilic gold and mica, the polymer formed large aggregates, whereas on hydrophobic HOPG the polymers showed their chain morphology for single-molecule analysis (Supplementary Fig. 9, Methods). HOPG was chosen for detailed analysis since, besides preserving polymeric structure, it also mimics the hydrophobicity of the diamond crystal used for the FTIR structural analysis.

AFM morphology maps on HOPG showed significant differences in shape and size of χ - versus *rac*-polymers (Fig. 4a, Supplementary Fig. 10). A single-molecule statistical analysis of the volume of the polymers was conducted to estimate their molecular weight and polydispersity (Supplementary Note 5). The χ -polymers had AFM-measured molecular weight of 232 ± 139 kDa and PDI-1.36; while the *rac*-polymers had higher molecular weight of 1219 ± 1003 kDa and PDI-1.68. The comparison of single-molecule AFM and bulk GPC data (Fig. 4b, Supplementary Fig. 2) demonstrated that χ -polymers maintained a single-chain conformation, while the *rac*-polymers self-assembled on the surface.

Ultra-high resolution AFM 3D imaging was further performed to unravel the topological structure of single *rac*- and χ -polymer chains. The AFM maps and the height cross-sectional profile of χ -polymer chains showed a helical structure (Fig. 4c, Supplementary Fig. 11). The *rac*-polymers did not show any periodic structure at the single-chain level (Fig. 4d). To quantitatively assess the presence of a helical structure in χ - vs. *rac*-polymers, we calculated the Fast Fourier Transform (FFT) of the cross-sectional profiles of the single-chains against any possible residual periodicity on the HOPG surface (Supplementary Fig. 11–12). The FFT power spectra confirmed that χ -polymers had helical periodicity of ~40 nm, while single-chains of *rac*-polymers had no backbone periodicity.

Although *rac*-polymers did not have helical conformation, the AFM analysis showed that *rac*-polymers further self-assembled into ordered and periodic structures (Fig. 4a, e). To unravel the supramolecular order of these *rac*-assemblies, we performed a single-molecule analysis of their shape as a function of their increasing size (Fig. 4e). The smallest and most abundant *rac*-assemblies showed: a constant height of ~0.4 nm (Supplementary Fig. 11), which is the typical height of an organic chain on a surface; a transversal periodicity increasing in multiples of ~15 nm (Fig. 4f), corresponding to the convoluted width of a single chain. This analysis indicated that the *rac*-polymers initially self-assemble via lateral interactions of single-chains, which further assembly into larger supramolecular species with increasing height (Fig. 5).

Overall, the AFM single-molecule analysis was in excellent agreement with the IR structural results. AFM demonstrated that the χ -polymers have a helical backbone structure, in agreement with the C=O shift at lower wavenumber and increased IR absorption at 1656 cm^{-1} , which is a typical signature of helices in (bio)-polymers. It

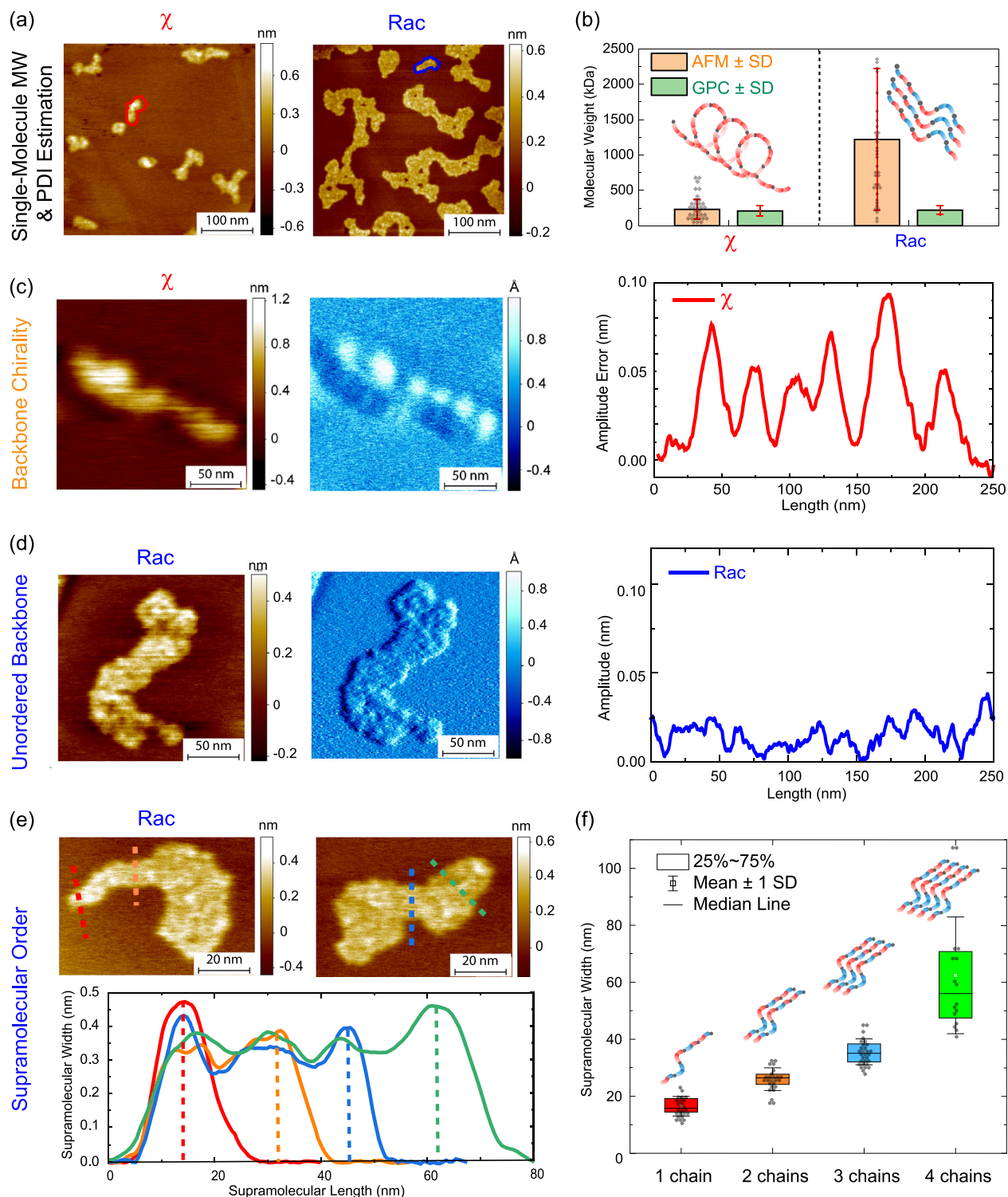
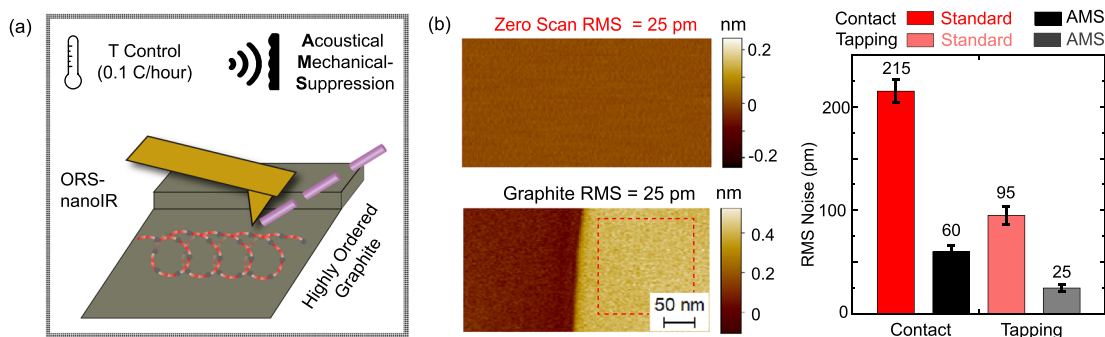


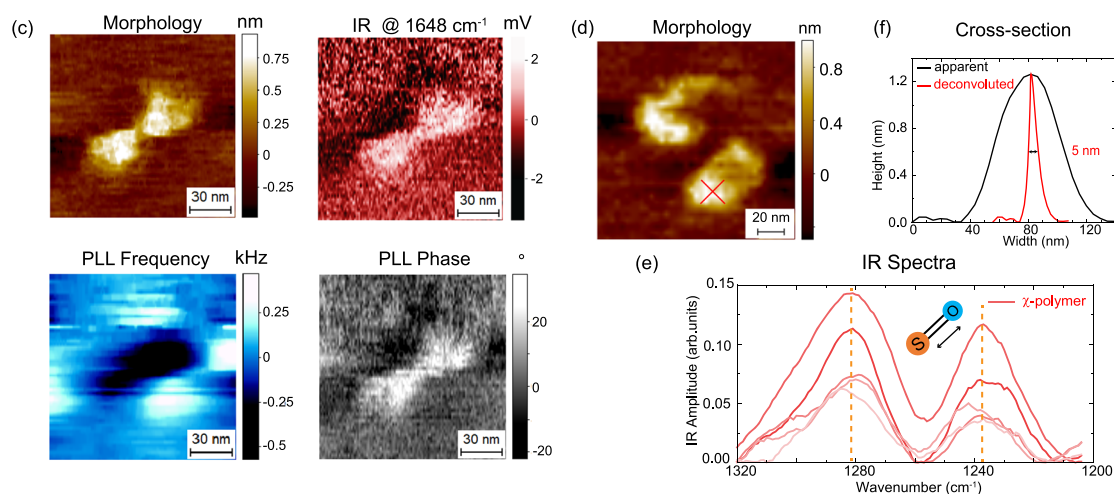
Fig. 4 | Nano-imaging analysis of morphology and supramolecular assembly state of χ - and rac-polymer chains. **a** AFM morphology maps of χ - (left) and rac-polymers (right). **b** Box plot comparing single-molecule volume-based molecular weight and polydispersity estimations by AFM (orange) and bulk GPC measurements (green) for χ - (left, $n = 33$) and rac-polymers (right, $n = 42$); error bars represent SD. Ultra-high resolution AFM of morphology (brown-yellow) and amplitude error (blue) of single polymeric chains for (c) χ -polymer and

(d) rac-polymer chains, together with their cross-sectional profile (smoothed using 3 pixels adjacent averaging, and a 7-points, 2nd order Savitzky-Golay filter). **e** AFM morphology map and cross-sectional profiles of the supramolecular assemblies of rac-polymers, made of one (red), two (orange), three (blue), four (green) chains. **f** Box plot comparing the cross-sectional width of single (red) and assembled two (orange), three (blue), and four (green) rac-polymer chains ($n = 96$); each data point is the width of a polymer, and box plot has one SD as whiskers.

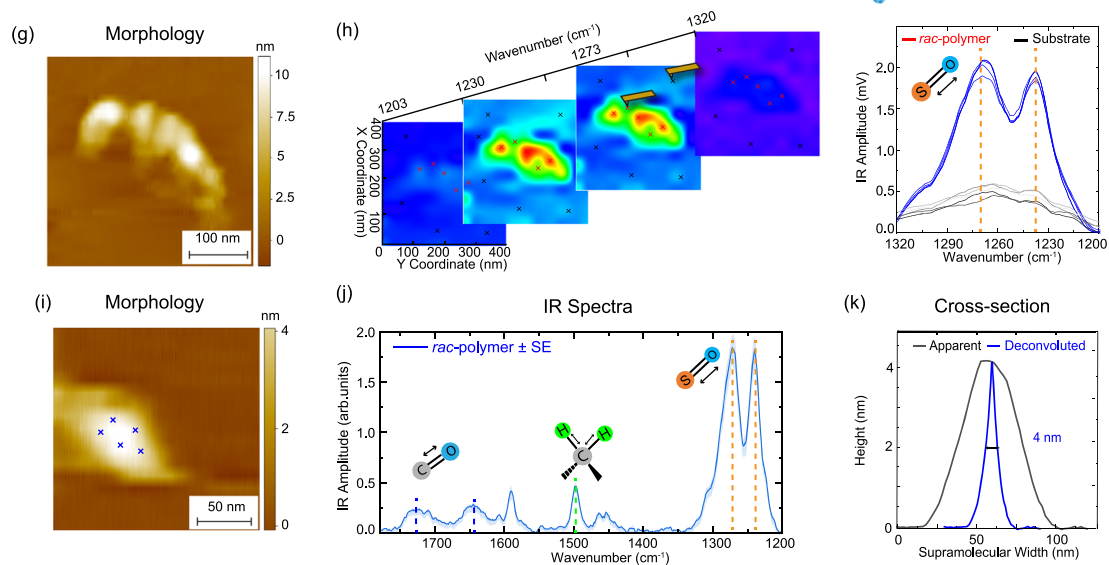
Chemical Analysis by AFM-IR with Sub-Å Noise Level



AFM-IR Analysis of Single Helical Polymer Chain on Graphite



AFM-IR Hyperspectral Analysis of Self-Assembled Racemic Chains



then showed that *rac*-polymers undergo self-assembly via lateral interactions; in agreement with FTIR conclusion that emergence of a new second C=O peak at 1723 cm⁻¹ could be associated to intramolecular π - π resonances in the RS/SR polymeric-units with a co-planar conformation and their supramolecular assembly via intermolecular π - π stacking. However, structural analysis of *rac*-polymers by AFM nano-imaging and IR structural analysis separately could not prove

directly whether the emerging C=O at 1723 cm⁻¹ had an intra- or inter-molecular origin. To unravel the origin of this structural signature, we further applied AFM-IR nano-chemical analysis.

Achieving Single Polymer Chain Nano-Chemical Analysis

Chemical-structural analysis of single polymer chains and assemblies paves the way for understanding the molecular origin of the

Fig. 5 | Nano-Chemical Imaging and Spectroscopy of Single Polymer Chains. **a** Schematic of the technological advances for acoustical mechanical suppression (AMS), which empowers chemical analysis with picometre-sensitivity by AFM-IR. **(b, left)** Morphology maps of bare HOPG in tapping mode in zero scan (top) and finite scan (bottom) by AMS AFM-IR (red-dashed box indicates area used for RMS calculation). **(b, right)** RMS noise of AFM-IR with and without AMS in tapping and contact modes; error bars represent sensitivity uncertainty and SE of three different areas within the same map. Single-chain χ -polymer nano-chemical analysis by AMS AFM-IR. **c** Morphology, IR amplitude, PLL frequency and PLL phase of a single polymer chain. **d** Morphological map of two single χ -polymer chains, with location

of single-molecule IR spectrum indicated (cross). **e** Cross-sectional and deconvoluted polymer profiles at the cross location. **f** IR Spectra acquired on the single polymer chains showing characteristic S = O peaks (red cross, **d**). Single-Chains rac-polymer nano-chemical analysis by AMS AFM-IR. **g** Morphology map of an assembly of a few single rac-polymer chains. **h** Left: Hyperspectral 4D plot (x-y coordinates, z-axis wavenumber, colour scale absorption intensity) with slices at 1203, 1240, 1273 and 1320 cm^{-1} . Right: Two sets of representative spectra (background and polymer indicated by AFM probe). **i** Morphology map of another assembly of single rac-polymer chains. **j** Corresponding IR spectra from marked positions (shading represents SE). **k** Cross-sectional and deconvoluted polymer profiles.

emergence of supramolecular order in the *rac*-polymers. However, to date, AFM-IR single-molecule sensitivity has been limited to molecules >400 kDa; and only if placed at a metallic nanogap between a gold surface and AFM probe. Indeed, the use of non-metallic substrates like HOPG would cause a further drop in AFM-IR sensitivity larger than 10-folds.

To allow the chemical analysis of single polymer chains of molecular weight down to ~200 kDa on non-metallic surfaces, such as HOPG, we developed acoustical-mechanical suppressed (AMS) AFM-IR with sub-Angstrom noise level (Fig. 5, Supplementary Fig. 13–14). AFM-IR works by detecting the photothermal expansion of a sample after its absorption of IR light. This detection mechanism is highly sensitive to external mechanical and acoustic noise, with typical frequencies between 0–500 Hz, which can propagate into the cantilever and reduce the signal-to-noise ratio of the detected photothermal signal (Supplementary Fig. 13)⁴⁹. We leveraged composite foams, with absorption frequencies between 0–4 kHz to isolate the surfaces of our instrument from ground oscillations (Fig. 5a, **Methods**). This isolation overall suppressed the noise transduced to the AFM cantilever, while measuring the photothermal signal. It thus allowed to achieve RMS noise of 25 ± 5 pm in tapping-IR and 60 ± 5 pm in contact-IR modes. The low level of noise in turn allows chemical-imaging of monoatomic steps of HOPG with ~3 Å height (Fig. 5b, Supplementary Fig. 13–14). To further allow single-molecule localisation with high-accuracy, we reduced AFM thermal drift by stabilising room temperature with variations <0.1 °C/h (Supplementary Fig. 13)⁵⁰.

We then applied AMS AFM-IR to extract structural information of single polymer chains from nano-resolved IR maps and spectra as in bulk FTIR. We first focused on χ -polymers (Fig. 5c–f). Tapping-IR allowed achieving multimodal imaging of morphology and IR absorption of a single polymer chain with a height down to ~5 Å (Fig. 5c); the phase locked loop (PLL) tracking of contact resonance frequency assured that chemical contrast was not affected by mechanical effects. Next, we pointed the AFM probe on a single polymer chain in the map (Fig. 5d) to acquire nano-localised IR spectra (Fig. 5e); for chains with a size down to ~0.8 nm height and ~5 nm width (Fig. 5f), corresponding to a molecular weight of ~200 kDa. While preserving better topography, tapping-IR detection was limited to the S=O region of a single χ -polymer chain by low signal-to-noise ratio (SNR).

We thus employed contact-IR mode to detect the chemical properties of *rac*-polymers (Fig. 5g–k, Supplementary Fig. 15). Figure 5g shows a representative *rac*-polymer assembly. Instead of single-wavenumber IR maps (Fig. 5c), we acquired 4D hyperspectral chemical maps of the polymers. Figure 5h shows four 3D-slices of the hyperspectral map, where each pixel represents an IR spectrum. The IR spectra showed the typical S=O absorption of the *rac*-polymer; while the HOPG surface showed significantly lower and uncorrelated IR absorption, which was subtracted to correct the spectra of the polymers (Supplementary Fig. 14–15). The high SNR allowed acquiring nano-localised spectra of single *rac*-polymer assemblies in the full 1800–1200 cm^{-1} fingerprint region (Fig. 5i, j), for assemblies with a size

down to ~4.5 nm in height and ~4 nm in width, corresponding to ~2–4 chains (Fig. 5k, Supplementary Fig. 15).

The emerging supramolecular C=O stretching at 1723 cm^{-1} was observed in all acquired IR spectra of different *rac*-assemblies (Supplementary Fig. 15), but with significant variations between different assemblies. We thus proceeded to a statistical analysis of their nano-chemical heterogeneity by AMS AFM-IR.

Unravelling the origin of the emergence of supramolecular chirality

We leveraged AFM-IR ultra-high sensitivity to investigate how the chemical signature of the *rac*-polymers varied as a function of their size and supramolecular state, to unravel if the emerging C=O at 1723 cm^{-1} is related to intra- or inter-molecular interactions (Fig. 6, Supplementary Fig. 15).

We acquired AFM-IR spectra from racemic polymer assemblies with varying size, from the smallest one (Fig. 6a, height ~4.5 nm; deconvoluted radius ~4 nm) to the largest ones (Fig. 6b, height ~10 nm; deconvoluted radius ~6 nm). Although at the limit of AFM-IR sensitivity, smaller assemblies showed lower IR signal than larger ones in accordance with Beer-Lambert Law (Fig. 6c, Supplementary Fig. 15).

To reduce spectral variability due to IR absorption intensity and perform a PCA analysis in the fingerprint region of protein (1750–1200 cm^{-1}), we normalized the IR spectra to their maximum. The PCA analysis showed that smaller (3.0–6.4 nm) and larger assemblies (7.5–15 nm) belong to separate spectroscopic clusters with 95% confidence (Fig. 6c). Significant part of the observed spectroscopic difference between the two clusters related to the conformation of the C=O group (Fig. 6e), thus indicating with statistical significance that *rac*-polymers of different sizes may have different structural properties.

To evaluate structural differences in the backbone and interactions between our *rac*-polymers, we consequently focused our analysis on the C=O groups (Fig. 6f, 1780–1600 cm^{-1}). Indeed, the emergence of the second C=O at 1725 cm^{-1} was associated by IR and UV-Vis with inter-molecular interactions in the *rac*-polymers. We normalised the spectra to the backbone C=O peak at 1646 cm^{-1} , to investigate the structural differences related to the emergent C=O peak at 1723 cm^{-1} ; independently of the number of C=O bonds present in the assemblies. The shape of the emergent C=O peak was significantly different for smaller assemblies compared to larger ones, as confirmed with 95% confidence by PCA analysis of the second derivatives of the spectra (Fig. 6g). The PC1 loading plot of the second derivatives proved with statistical significance (Fig. 6h, 81% variance) that larger assemblies had increased absorption of the emergent C=O peak compared to smaller assemblies. Moreover, larger assemblies showed a shift of the C=O maximum at higher wavenumber at 1730 cm^{-1} , compared to smaller assemblies having a lower absorption peak at 1710 cm^{-1} . Since we normalised the spectra to the backbone C=O peak (1646 cm^{-1}), these modifications could only be associated to an increasing number of intermolecular (π - π stacking) interactions between the *rac*-polymer chains in the larger assemblies; rather than a constant number of intramolecular interactions in the single chains.

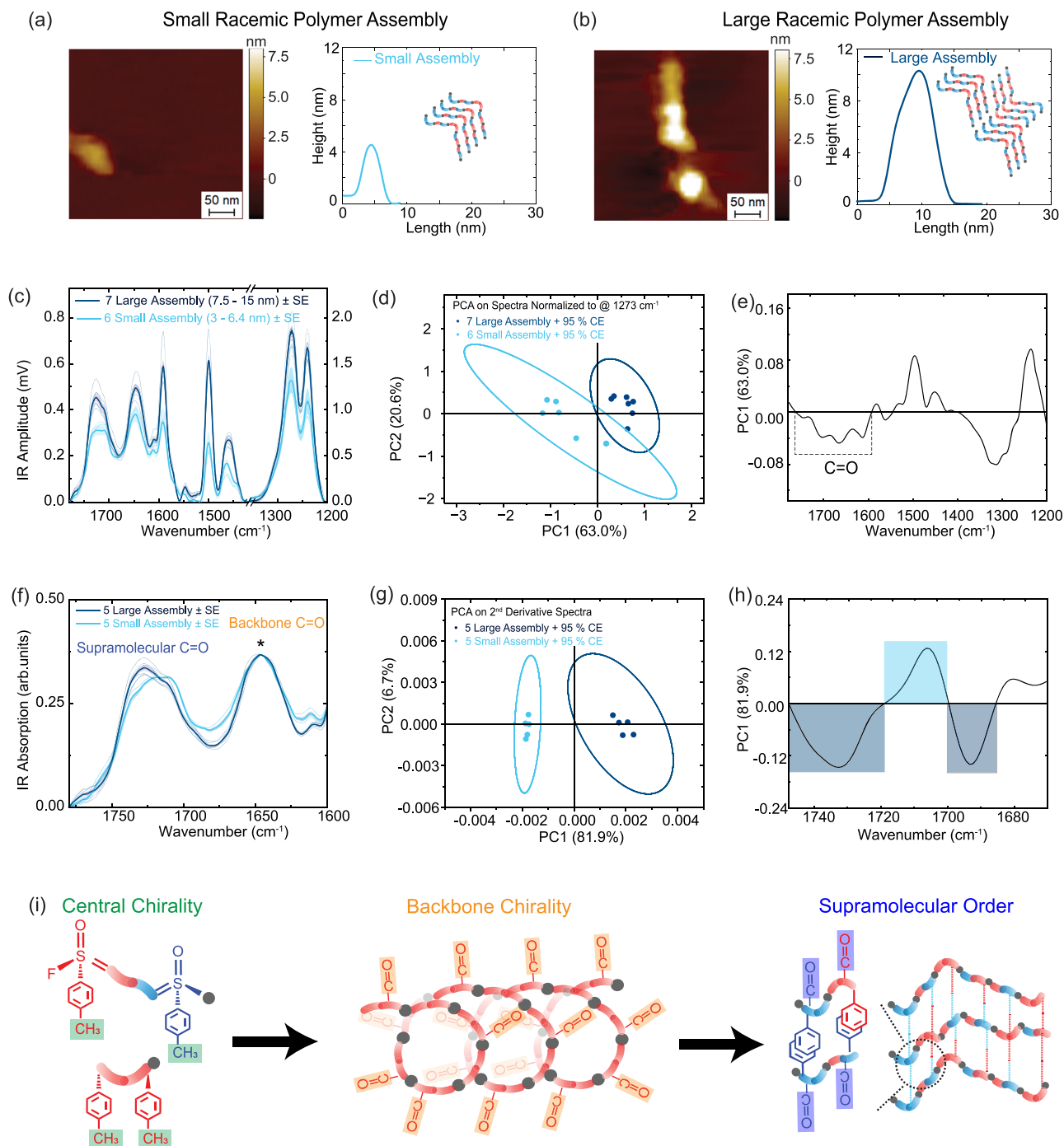


Fig. 6 | Nano-chemical analysis of the emergence of supramolecular chirality in heterogeneous rac-polymer assemblies. AFM Morphology maps of characteristic (a) large and (b) small racemic assembly. c AFM-IR spectra of several racemic assemblies normalized to 1273 cm^{-1} (Supplementary Fig. 15); shading represents SE. d Score plot of PCA analysis of the normalized spectra in c with 95% confidence ellipses (CE). e Loading plot of the spectra highlighting the molecular bonds related to the variance difference. f Zoomed spectra from 1780–1600 cm^{-1} , normalized to

1646 cm^{-1} (C=O peak); shading represents SE. g PCA Score Plot of second derivatives of spectra in f with 95% confidence ellipses (CE). h Loading plot of PC1 of the second derivatives highlighting the structural features of the small vs. large assemblies. i Schematic of the key molecular bonds used to identify and discriminate the emergence of different forms of chirality; from central chirality in molecules (CH_3), to backbone chirality in polymers (C=O at 1646 cm^{-1}), supramolecular order in assemblies (C=O at 1725 cm^{-1}).

Overall, AMS AFM-IR proved the ability of studying the heterogeneous chemical-structural properties of single polymeric assemblies, composed of only a few chains. The analysis enabled identifying the splitting of the C=O group absorption and the second peak at 1723 cm^{-1} as key signature of intermolecular π - π stacking, and of the emergence of supramolecular order and chirality in the *rac*-polymers (Fig. 6i). The single-molecule results provided by

AFM-IR were thus in excellent agreement with the independent spectroscopic evidence provided above by the IR and UV-Vis structural analysis.

Discussion

Despite over a century of investigations, the hierarchical emergence of chirality over multiple chemical and topological scales has remained

elusive due to technological limitations in characterizing different forms of chirality at the molecular nanoscale⁹.

To bridge this gap, we have elucidated the complex interplay between central chirality in small molecules and the emergence of backbone and supramolecular chirality in polymers from sub-molecular scales to macro-molecular scales. To reach this objective, we have developed acoustical-mechanical suppressed AFM-IR to achieve chemical-structural analysis of the heterogeneity and assembly of single-polymer chain(s). This ultra-high sensitivity, combined with nano-imaging and bulk spectroscopy, enabled distinguishing between different forms of chirality and their structural manifestation at the molecular level via bonds generally present and abundant in small molecules, polymers and their supramolecular assemblies (Fig. 6i). Introducing the concept of same connectivity, different chirality to discern and study different forms of chirality, we first identify the conformation of CH groups as a key signature of central chirality in small molecules. Second, we generalised the idea that C=O carbonyl is sensitive in polymers to backbone helical structure and self-assembly via π - π intermolecular stacking^{51,52}, as in the case of α -helical structure in single protein^{51,52} and supramolecular stacking and ordering during their assemblies^{14,15}.

Overall, the presented results contribute to understanding the hierarchical emergence of chirality in polymers and pose a new framework for offering key insights into the structural-chemical determinants of chirality across multiple scales. This understanding will be in turn fundamental for the rational design of advanced chiral materials with tailored properties and may help to accelerate the development of novel materials in electronics, chemical industry, biotechnology, and healthcare. Indeed, the concept of same connectivity, different chirality is not limited to synthetic polymer systems, but can be generalized to other chemistries, allowing for modular design and stereospecific control. For example, backbone chirality also underlies protein secondary structures such as α -helices and β -sheets, which are crucial for the tertiary organization of human-designed proteins and their functionality⁵³.

Finally, this study pushes the limits of nano-analytical chemistry down to the identification of the molecular fingerprint and the structural analysis of a single polymer chain on any surface, without requiring the enhancement of metallic surfaces. These capabilities pave the way to have a new single-molecule and angstrom-resolved window of observation into the chemical-structural properties of virtually any (bio-)organic material in nature.

Methods

General conditions of materials synthesis

All commercial chemicals were used as received and stored under argon. Reagents were used without further purification unless otherwise noted³⁵. Unless otherwise noted, all reactions were performed using glassware without further preparation. Certain reactions were carried out under anhydrous conditions. For these reactions, glassware was oven-dried at temperatures exceeding 100 °C for at least 5 h, or was dried under vacuum with a heat gun ($T > 200$ °C), under oxygen-free and water-free conditions.

After weighing any solids, the glassware was connected to a Schlenk line and then placed under vacuum and flushed with nitrogen gas (3 \times purged). Liquids were added via a syringe through a rubber stopper. The following solvent abbreviations are used: n-hexane (n-hex), tetrahydrofuran (THF), ethyl acetate (EA), N,N-dimethylformamide (DMF), and petroleum ether 40–60 (P.E.). For HPLC and GPC analysis, all solvents were purchased from Biosolve®. Extra-dry solvents were purchased from Acros Organics. Commercial solvents were obtained from Honeywell. These solvents were used as received without any distillation.

All reagents were used as received, following the procedure we have used in a previously published method from our group:

Benzenesulfonic acid sodium salt (98%), 1,8-diazabicyclo[5.4.0]undec-7-ene (98%), sodium hydride (60% dispersion in mineral oil), 4,4'-oxybis(benzoic acid) (99%), bisphenol A ($\geq 99\%$), were purchased from Merck Life Science N.V. Oxalyl chloride (98%), p-toluenesulfonic acid sodium salt (97%), triphenyl phosphine (99%), methyl iodide (99%) and potassium carbonate ($\geq 99\%$) were purchased from Fisher Scientific B.V. and Selectfluor (98%) were purchased from Fluorochem Ltd. Flash column chromatography was performed using a Biotage® system using Sili-Cycle® precast silica columns (200–300 mesh or 300–400 mesh). TLC analysis was performed on pre-coated, alumina-backed silica gel plates. TLC plates were analyzed by UV fluorescence (254 nm) or I_2 staining.

Synthesis of monomers

Synthesis of N',N''-(4,4'-oxybis(benzoyl))bis(4-methylbenzenesulfonimidoyl fluoride) (**rac-monomers**) and N'(R),N''(R)-(4,4'-oxybis(benzoyl))bis(4-methylbenzenesulfonimidoyl fluoride) (**χ -monomers**) were synthesized by reacting 4,4'-oxybis(N-(p-tolylsulfonyl)benzamide) with NaH in THF to form an intermediate, which is then treated with Selectfluor and KOAc in EtOH at 0 °C to room temperature³⁵.

Characterisation of monomers

To characterize the purity of the **monomers**, we performed NMR and HMRS analysis, as reported below:

rac-monomers. ¹H NMR (400 MHz, CDCl₃): δ 8.18 (d, J = 8.5 Hz, 4H), 8.08 (d, J = 8.1 Hz, 4H), 7.48 (d, J = 8.1 Hz, 4H), 7.08 (d, J = 8.5 Hz, 4H), 2.53 (s, 6H); (**SI Data Set**)

¹³C NMR (101 MHz, CDCl₃): δ 169.2, 160.5, 147.2, 132.3, 131.6 (d, J = 20 Hz), 130.3, 129.9, 128.0, 118.6, 21.8. (**SI Data Set**)

HRMS (ESI) m/z : [M+Na]⁺ calc. for C₂₈H₂₂F₂N₂O₅S₂Na: 591.0830, found: 591.0834. (**SI Data Set**)

χ -monomers. ¹H NMR (400 MHz, CDCl₃): δ 8.09 (d, J = 8.5 Hz, 4H), 7.98 (d, J = 8.1 Hz, 4H), 7.36 (d, J = 8.1 Hz, 4H), 6.98 (d, J = 8.5 Hz, 4H), 2.42 (s, 6H); (**SI Data Set**)

¹³C NMR (101 MHz, CDCl₃): δ 169.2, 160.5, 147.2, 132.3, 131.6 (d, J = 20 Hz), 130.3, 129.9, 128.0, 118.6, 21.9. (**SI Data Set**)

HRMS (ESI) m/z : [M+Na]⁺ calc. for C₂₈H₂₂F₂N₂O₅S₂Na: 591.0830, found: 591.0830. (**SI Data Set**)

Synthesis of the polymers

The polymer was synthesized with slight modifications as follows. In a 2 mL Biotage microwave glass vial containing a magnetic stir bar, bis(4-methylbenzene sulfonimidoyl fluoride) **1** (100 mg, 1.0 equiv.) and disodium bis-phenolate **2** (47.9 mg, 1.0 equiv.) were added inside an argon-filled glovebox (MBRAUN's MB 20 G-LMF gas purifier with H₂O and O₂ values of <0.1 ppm)³⁵. The vial was placed on a magnetic stirring plate, and 1.00 mL of anhydrous acetonitrile (Acros organics 99.9 + % Extra Dry over Molecular Sieve, AcroSeal®) and 1.00 mL of anhydrous N,N-dimethylformamide (Acros organics 99.9 + %, absolute, over molecular sieves (H₂O \leq 0.01%), $\geq 99.8\%$ (GC), AcroSeal®) were added with vigorous stirring. The vial was then sealed with caps. The polymerizations were heated at 80 °C. After stirring at 80 °C in the glovebox for approximately 24 h, the glass vial was removed from the glovebox, and 0.5 mL of DMF was added. The vial was shaken to facilitate dissolution, and the resulting solution was slowly poured into 50 mL of MeOH while continuously stirring. After precipitation occurred, the stirring was continued for an additional 10 min. After allowing the formed precipitate to settle for 10 min, the methanol layer was removed, and a minimal amount of DMF was added to redissolve the precipitate. This cycle of precipitation, sedimentation, and redissolution was repeated four times. The resulting white powder/fibrous material was transferred to a 4 mL glass vial and dried at 50 °C under vacuum for a minimum of 12 h. GPC measurements of the resulting polymers were conducted using a DMF:LiBr (0.1%) mixture as the eluent solvent.

Characterisation of polymers

To characterize the purity of the polymers, we performed NMR analysis. The results are reported below:

rac-polymers. ¹H NMR (400 MHz, CDCl₃): δ 8.04 (d, *J* = 8.0 Hz, 4H), 7.86 (d, *J* = 8.0 Hz, 4H), 7.27 (d, *J* = 8.0 Hz, 4H), 6.99 (d, *J* = 8.0 Hz, 4H), 6.93 (d, *J* = 8.0 Hz, 8H), 2.39 (s, 6H), 1.50 (s, 6H); (SI Data Set)

¹³C NMR (101 MHz, CDCl₃): δ 170.88, 160.07, 149.32, 145.48, 133.48, 132.27, 131.90, 130.91, 130.30, 129.92, 128.18, 128.02, 122.31, 118.32, 42.66, 30.77, 21.86, 21.75. (SI Data Set)

χ-polymers. ¹H NMR (400 MHz, CDCl₃): δ 8.04 (d, *J* = 8.0 Hz, 4H), 7.86 (d, *J* = 8.0 Hz, 4H), 7.27 (d, *J* = 8.0 Hz, 4H), 7.00 (d, *J* = 8.0 Hz, 4H), 6.93 (d, *J* = 8.0 Hz, 8H), 2.37 (s, 6H), 1.51 (s, 6H); (SI Data Set)

¹³C NMR (101 MHz, CDCl₃): δ 170.89, 160.06, 149.32, 147.17, 145.68, 133.44, 132.32, 131.90, 130.89, 130.30, 129.92, 128.18, 128.02, 122.31, 118.57, 118.32, 67.99, 42.66, 30.78, 25.62, 21.88, 21.77. (SI Data Set)

¹⁹F NMR (376 MHz, CDCl₃): δ 65.25. (SI Data Set)

Synthesis of modified monomers and repeating units

Synthesis of 4-(2-(4-methoxyphenyl)propan-2-yl)phenol (link-monomers with a methyl cap): An oven-dried 250 mL round-bottomed flask was prepared with a magnetic stirbar and a rubber septum. The flask was charged with Bisphenol-A (5.0 gm, 21.9 mmol) was dissolved in dry DMF (50 mL), followed by the addition of potassium carbonate (3.0 gm, 21.9 mmol). The mixture was cooled to 0 °C with an ice bath, and a solution of methyl iodide (3.1 gm, 21.9 mmol) was added dropwise over 5 min. The mixture was stirred at 0 °C for approximately 2 h and then left to stir overnight. The reaction was then diluted with water (10 mL) and extracted with EtOAc (15 mL × 2). The combined organic layers were washed with water (15 mL × 2), saturated aqueous NaCl (15 mL), and dried over anhydrous sodium sulfate. The solvent was removed, and the crude material was purified by flash chromatography on silica gel (petroleum ether: ethyl acetate 8:2) to afford 5.1 g (96%) of 4-(2-(4-methoxyphenyl)propan-2-yl)phenol (**link-monomers with a methyl cap**) as a colourless oil.

Synthesis of 4-(2-(4-methoxyphenyl)propan-2-yl)phenyl N-(4-(4-(fluoro(oxo)(p-tolyl)-l6-sulfaneylidene)carbamoyl)phenoxy)benzoyl)-4-methylbenzenesulfonimide (rac-repeating units) and/or 4-(2-(4-methoxyphenyl)propan-2-yl)phenyl (S)-N-(4-(4-(fluoro(oxo)(p-tolyl)-l6-sulfaneylidene)carbamoyl)phenoxy)benzoyl)-4-methylbenzenesulfonimide (χ-repeating units): **rac-repeating units** and **χ-repeating units** were synthesized according to a protocol adapted from the literature³⁴. In brief: a 100 mL round-bottomed flask was dried in an oven and fitted with a rubber septum and a magnetic stirbar. To the flask, 25.0 mg (0.044 mmol) of SuFEx (**χ-monomers** or **rac-monomers**) compound and 10.6 mg (0.044 mmol) of 4-(2-(4-methoxyphenyl)propan-2-yl)phenol (**link-monomers with a methyl cap**) were added in 1 mL dry THF, followed by the addition of 2.0 mg (0.044 mmol) of Sodium hydride (60% in oil). The mixture was stirred under argon at room temperature and monitored by thin layer chromatography (TLC). The reaction was stopped by adding 10 mL of water and the resulting mixture was extracted with CH₂Cl₂ (3 × 50 mL). The organic phase was dried using anhydrous MgSO₄ and the crude product was purified by column chromatography on silica gel, using a mixture of EtOAc and n-hexane in the ratio of 1:19 to 1:4 as the eluent. The final yield was 24 mg of 70% (**rac-repeating units**) or 26 mg of 75% (**χ-repeating units**), and both obtained as white solids.

Characterisation of repeating units

To characterize the purity of the **repeating units**, we performed NMR and HRMS analysis. The results are reported below:

rac-repeating units. ¹H NMR (400 MHz, CDCl₃): δ 8.16–8.12 (m, 4H), 8.07 (d, 2H, *J* = 8.0 Hz), 7.96 (d, 2H, *J* = 8.0 Hz), 7.46 (d, 2H, *J* = 8.0 Hz),

7.37 (d, 2H, *J* = 8.0 Hz), 7.16 (d, 2H, *J* = 8.0 Hz), 7.08–7.00 (m, 8H), 6.79 (d, 2H, *J* = 8.0 Hz), 3.77 (s, 3H), 2.51 (ss, 6H), 1.61 (s, 6H). (SI Data Set)

¹³C NMR (101 MHz, CDCl₃): δ 171.00, 169.38, 160.98, 159.80, 157.73, 150.49, 147.29, 147.07, 145.73, 142.29, 133.66, 132.46, 132.42, 132.08, 131.39, 130.42, 130.03, 129.67, 128.37, 128.19, 128.15, 127.83, 122.27, 118.72, 118.43, 113.51, 55.35, 42.31, 31.06, 29.85, 22.02, 21.90. (SI Data Set)

¹⁹F NMR (376 MHz, CDCl₃): δ 65.27. (Supplementary Fig. 3)

HRMS (ESI) m/z: [M + H]⁺ + calc. for C₄₄H₄₀O₇N₂F₂: 791.2255, found: 791.2256. (SI Data Set)

χ-repeating units. ¹H NMR (400 MHz, CDCl₃): δ 8.16–8.12 (m, 4H), 8.07 (d, 2H, *J* = 8.0 Hz), 7.96 (d, 2H, *J* = 8.0 Hz), 7.46 (d, 2H, *J* = 8.0 Hz), 7.38 (d, 2H, *J* = 8.0 Hz), 7.16 (d, 2H, *J* = 8.0 Hz), 7.08–7.00 (m, 8H), 6.79 (d, 2H, *J* = 8.0 Hz), 3.77 (s, 3H), 2.51 (ss, 6H), 1.61 (s, 6H). (SI Data Set)

¹³C NMR (101 MHz, CDCl₃): δ 170.97, 169.35, 161.00, 159.81, 157.76, 150.49, 147.28, 147.10, 145.71, 142.30, 133.74, 132.42, 132.08, 131.79, 131.43, 130.42, 130.02, 129.71, 128.38, 128.20, 128.15, 127.84, 122.27, 118.72, 118.43, 113.54, 55.35, 42.32, 31.07, 29.85, 22.01, 21.90. (SI Data Set)

¹⁹F NMR (376 MHz, CDCl₃): δ 65.27. (SI Data Set)

HRMS (ESI) m/z: [M + H]⁺ + calc. for C₄₄H₄₀O₇N₂F₂: 791.2252, found: 791.2256. (SI Data Set)

NMR measurements

A Bruker Avance III 400 MHz spectrometer was used to record ¹H NMR, ¹³C NMR, and ¹⁹F NMR spectra at a temperature of 298 K. The chemical shifts are listed in ppm on the δ scale and coupling constants were recorded in Hertz (Hz). The ¹⁹F NMR was not referenced. All other chemical shifts are calibrated relative to the signals corresponding of the non-deuterated solvents (CHCl₃: δ = 7.26 ppm for ¹H and 77.16 ppm for ¹³C, DMSO: δ = 2.50 ppm for ¹H and 39.52 ppm for ¹³C, CH₃CN: δ = 1.94 ppm for ¹H and 1.32 and 118.26 ppm for ¹³C). Abbreviations are used in the description of NMR data as follows: chemical shift (δ = ppm), multiplicity (s = singlet, d = doublet, t = triplet, q = quartet, dt = doublet of triplets, m = multiplet, br = broadened), coupling constant (*J*, Hz).

HR-MS measurements

The Quadrupole Time-of-Flight (QTOF) micro-spectrometer (Thermo Fisher Scientific Inc., United States) was used to obtain high-resolution mass spectra (HR-MS) through electrospray ionization (ESI) in either positive mode (ESI+) or negative mode (ESI-).

HPLC measurements

Enantioselectivity was monitored using high-performance liquid chromatography (HPLC, Agilent 1100 bearing a UV-Vis detector) with a CHIRALPAK[®] IA column (5 μm, 4.6 mm × 250 mm). As references, racemic products or nonchiral mixtures, including diastereoisomers, were synthesized to determine the column conditions for baseline separation. Unless specifically mentioned, these were found to be n-hexane/dichloromethane/iso-propanol (80/20/2.5) as the mobile phase, a flow rate of 0.5 mL/min, room temperature, and a detector wavelength of 240 nm.

GPC measurements

Gel Permeation Chromatography (GPC) was performed using an Agilent Technologies 1200 system, equipped with a diode-array detector (DAD, G1315D), a refractive index detector (RID, G1362A), autosampler (ALS, G1329A), bin pump (G1312A), solvent degasser (G1322A), and a VARIAN GPC/SEC column from PLgel 5 μm MIXED-D (300 × 7.5 mm). The system was calibrated with EasyVial PS-M and EasyVial PS-L polystyrene standards (Agilent Technologies), GPC polystyrene standards with a combined range from Mp 400 to 2,000,000 Da (Fluka). HPLC-grade tetrahydrofuran (THF, Biosolve[®], unstabilized, HPLC grade) was

used as a mobile phase for low molecular weight polymers, and high molecular weight polymers were measured using HPLC grade N,N-Dimethylformamide (DMF, Biosolve®, unstabilized, HPLC grade) with 0.1% LiBr (ReagentPlus®, ≥99% from Sigma-Aldrich). All GPC measurements were performed at room temperature or at 25 °C using an injection volume of 10 µL (1.0 mg/mL). The polymer number average molecular weight (M_n) and polydispersity (\bar{D}) relative to a set of polystyrenes were determined using DAD (at 270 nm or 290 nm) or RI detectors.

FTIR measurements, Data Treatment and Analysis

Attenuated total reflection infrared spectroscopy (ATR-FTIR) was performed using a Bruker Tensor 27 IR equipped with Platinum ATR accessory with a diamond ATR element. Spectra were collected by the built-in software OPUS (version 7.8, Bruker, USA). The samples were deposited on the ATR crystal by 2 times of 0.5 µL droplet at a concentration of 2 mg·mL⁻¹ in THF. Spectra were acquired at the range of 3500 cm⁻¹–500 cm⁻¹ with a resolution of 4 cm⁻¹. All spectra were processed using OriginPro (version 2022b, OriginLab, USA). For each sample, 5 spectra of 512 co-averages were collected. Since the spectral background line shape slightly depends on wavenumber regions and at lower wavenumber range (2500–500 cm⁻¹ range) and the higher wavenumber range (3500–2500 cm⁻¹ range) does not share the same baseline. The spectra were first cut into two ranges that contains relevant information: lower wavenumber range (1800–1000 cm⁻¹ range) and higher wavenumber range (3150–2700 cm⁻¹ range). The final spectra for each range were obtained by averaging 5 individual spectra. Each spectrum was smoothed using a Savitzky–Golay filter (second order, 7pts), baseline-corrected (zero-order for 1800–1000 cm⁻¹ range and first-order for 3150–2700 cm⁻¹ range), and normalizing to the range [0,1].

Circular dichroism measurements

Circular Dichroism (CD) measurements were done on a Jasco J-715 spectropolarimeter equipped with a Peltier holder. CD spectra were measured at a concentration of 20 µg·mL⁻¹ in a Hellma® Quartz Glass high performance macro absorption cell with a 0.1 cm pathlength. Measurements were performed with a scanning speed of 50 nm·min⁻¹ with a data pitch of 0.5 nm at 20 °C and were averaged from 16 scans. All spectra were processed using OriginPro (version 2022b, OriginLab, USA). The final spectra were obtained by first subtraction of THF background, secondly, applying a Savitzky–Golay filter (second order, 21 pts) and finally converting to molar ellipticity by the following formula: $= \frac{M \times \theta_{obs}}{10cl}$, where M is averaged molecular weight in g·mol⁻¹, l is the path length (0.1 cm) and c is the concentration [mg·mL⁻¹].

UV-Vis Measurements

UV-Vis measurements were done on a Shimadzu UV-2600 spectrometer. Spectra were measured in THF with a Hellma® Quartz Glass high performance macro absorption cell with a 0.1 cm pathlength. Measurements were performed in the range of 185–600 nm with a scanning speed of 1 nm·s⁻¹ with a data pitch of 1 nm, at room temperature, and with 16 co-averages. All spectra were processed using OriginPro (version 2022b, OriginLab, USA).

AFM Sample Preparation

Samples deposition for atomic force microscopy (AFM) analysis was performed on three differently charged substrates: hydrophobic highly ordered pyrolytic graphite (HOPG), negative charged Mica and positive gold. Sample preparation was realized by two different methods: manual deposition and vacuum drying. For manual deposition, a 10 µL droplet of 2 µg/mL polymers solution in THF was applied at room temperature for 40 seconds on substrate. After the incubation time on the surface, then the sample was rinsed with 1 mL Milli-Q water and dried with a gentle flow of nitrogen gas. For Vacuum drying, a 10 µL

droplet of 2 µg/mL polymers solution in THF was applied at room temperature for 3 seconds on substrate under vacuum.

AFM Measurements

Atomic force microscopy (AFM) measurements were performed on a NX10 AFM (Park systems, South Korea) operating in True Non-Contact™ Mode with a silicon tip PPP-NCSTR (Park systems, nominal spring constant 7.4 Nm⁻¹, nominal tip radii ~7 nm). The image was acquired with a tip velocity of 0.8 µm per second. Three map sizes and two pixelization setting were employed: 4 × 4 µm² with 4 nm/px, 1 × 1 µm² and 0.5 × 0.5 µm² with 0.5 nm/px. Image flattening and cross-sectional dimension analysis of single polymers chains were performed by SPIP (Image Metrology, Denmark) software. We initially optimised the deposition of the polymers on three substrates with different charges: positive gold, negative mica, hydrophobic Highly Oriented Pyrolytic Graphite (HOPG) (Supplementary Fig. 8). HOPG was chosen as a substrate for high-resolution imaging because of its atomically flat surface, favourable interactions with hydrophobic polymers, and similar hydrophobicity as the diamond ATR-FTIR crystal, thus allowing to compare the molecules' behaviour on the surface. Each image was first flattened with a first-order polynomial fit for the global correction, and then, a zero-order least mean square (LMS) fit line-wise correction. Afterwards, the image was further flattened by first and second order LMS fit line-wise correction with area of interest masked.

Acoustical-mechanical suppressed AFM-IR

AFM-IR is based on the mechanical detection of the photothermal expansion of a sample when absorbing IR light. To achieve AMS AFM-IR, we leveraged composite foams to suppress any source of mechanical and acoustic noise transmission caused by cables and vibrating parts inside and outside our AFM-IR system, as well as mechanical noise transmission from the ground (Fig. 5a). Adhesive PUR Foam Acoustic Insulation (RS PRO, Netherlands) was applied directly under and on surface of the components of instrument to block the transmission of acoustic vibrations. To shield the controllers from vibrations, we used a double layer of foams: TC2 (EASYfoam, Netherlands) designed for broad-frequency cut-off from 500 Hz to 4 kHz; and PU (EASYfoam, Netherlands), with similar absorption values but with fire and water isolation for safety reasons. For ground noise isolation, we used EASYbond Trillingsisolatie (EASYfoam, Netherlands) with density of 140 kg/m³ to create a floating floor and dampen mechanical vibrations. The noise suppression was quantified on the acquired AFM-IR maps via their RMS noise and the integration of their FFT spectral noise within 0–500 kHz (Supplementary Fig. 13). In tapping mode, AMS AFM-IR achieved RMS noise level of 25 ± 5 pm to allow imaging single monoatomic steps of HOPG with a height of ~3 Å (Fig. 5b). In contact mode, the AMS suppression led to RMS down to 60 ± 5 pm, against a standard RMS noise of 215 ± 15 pm. To further allow single-molecule localisation with high-accuracy, we stabilised room temperature with variations below 0.1 °C per hour to reduce AFM thermal drift (Supplementary Fig. 13).

AFM-IR measurements, maps treatment and analysis

Analysis by AFM-IR was performed with a nanoIR3 (Bruker, USA) on atomically flat HOPG substrates. The substrate roughness and chemical response were also characterized by AFM-IR in the Supplementary Fig. 13. The root mean square roughness of the AFM maps was measured by SPIP (Image metrology, Denmark). The morphology of the polymer samples was scanned by the nanoIR microscopy system, with a line scan rate within 0.1–0.5 Hz and in contact mode. All AFM maps were acquired with a resolution between 1–30 nm/pixel. A silicon gold-coated PR-EX-nIR2 (Bruker, USA) cantilever with a nominal radius of ~30 nm and an elastic constant of about 0.2 N/m was used. The AFM images were treated and analysed using SPIP software. The height images were corrected using a first order polynomial flattening.

All measurements were performed at room temperature under controlled nitrogen atmosphere with relative humidity below 3%. Both spectra and images were acquired by using phase loop (PLL) tracking of contact resonance, the phase was set to zero to the desired resonant frequency around the IR amplitude maximum, and tracked with an integral gain $I = 0.2$ and proportional gain $P = 1$.

Data availability

All data needed to evaluate the conclusions in the paper are present in the paper and/or the Supplementary Information. Source data are provided with this paper. The source data underlying Figs. 1–6 and Supplementary Figs. 1–15 are provided as a Source Data file. Additional data are available from corresponding authors upon request. Source data are provided with this paper.

References

- Liu, M., Zhang, L. & Wang, T. Supramolecular chirality in self-assembled systems. *Chem. Rev.* **115**, 7304–7397 (2015).
- Adawy, A. Functional chirality: from small molecules to supramolecular assemblies. *Symmetry* **14**, 292 (2022).
- Sessler, J. L., Lawrence, C. M. & Jayawickramarajah, J. Molecular recognition via base-pairing. *Chem. Soc. Rev.* **36**, 314–325 (2007).
- Geider, K. & Hoffmannberling, H. Proteins controlling the helical structure of DNA. *Annu. Rev. Biochem.* **50**, 233–260 (1981).
- William, F. et al. De Novo design and structural characterization of proteins and metalloproteins. *Annu. Rev. Biochem.* **68**, 779–819 (1999).
- Xia, X. et al. Material choice and structure design of flexible battery electrode. *Adv. Sci.* **10**, 2204875 (2023).
- Zhang, L., Wang, H.-X., Li, S. & Liu, M. Supramolecular chiroptical switches. *Chem. Soc. Rev.* **49**, 9095–9120 (2020).
- Pop, F., Zigon, N. & Avarvari, N. Main-group-based electro- and photoactive chiral materials. *Chem. Rev.* **119**, 8435–8478 (2019).
- Buhse, T. et al. Spontaneous deracemizations. *Chem. Rev.* **121**, 2147–2229 (2021).
- Ikai, T., Kurake, T., Okuda, S., Maeda, K. & Yashima, E. Racemic monomer-based one-handed helical polymer recognizes enantiomers through auto-evolution of its helical handedness excess. *Angew. Chem. Int. Ed.* **60**, 4625–4632 (2021).
- Li, P., Gao, H., Zhao, B. & Deng, J. Enantioselective induction, amplification, and storage of helical chirality in absolutely achiral polymer systems. *Chem. Mater.* **34**, 7503–7515 (2022).
- Zha, X. et al. Modulating the macroscopic helicity of Poly(m-phenylenediamine) by achiral monomer copolymerization. *Adv. Funct. Mater.* **33**, 2211956 (2023).
- Wang, H. F. et al. Generalizing the effects of chirality on block copolymer assembly. *Proc. Natl Acad. Sci. USA* **116**, 4080–4089 (2019).
- Hall, V., Sklepari, M. & Rodger, A. Protein secondary structure prediction from circular dichroism spectra using a self-organizing map with concentration correction. *Chirality* **26**, 471–482 (2014).
- Barth, A. Infrared spectroscopy of proteins. *Biochim. Biophys. Acta* **1767**, 1073–1101 (2007).
- Kurouski, D. Advances of Vibrational Circular Dichroism (VCD) in bioanalytical chemistry. A review. *Anal. Chim. Acta* **990**, 54–66 (2017).
- Ruggeri, F. S. et al. Infrared nanospectroscopy characterization of oligomeric and fibrillar aggregates during amyloid formation. *Nat. Commun.* **6**, 7831 (2015).
- Han, Y. et al. Synthesis of chiral sequence-defined oligomers via sulfur–fluoride and sulfur–phenolate exchange reactions. *Nat. Synth.* <https://doi.org/10.1038/s44160-025-00805-8> (2025).
- Schwartz, J. J., Jakob, D. S. & Centrone, A. A guide to nanoscale IR spectroscopy: resonance enhanced transduction in contact and tapping mode AFM-IR. *Chem. Soc. Rev.* **51**, 5248–5267 (2022).
- Wang, F., Gnewou, O., Solemanifar, A., Conticello, V. P. & Egelman, E. H. Cryo-EM of Helical Polymers. *Chem. Rev.* <https://doi.org/10.1021/acs.chemrev.1c00753> (2022).
- Egelman, E. H. & Wang, F. Cryo-EM is a powerful tool, but helical applications can have pitfalls. *Soft Matter* **17**, 3291–3293 (2021).
- Kumaki, J., Sakurai, S.-I. & Yashima, E. Visualization of synthetic helical polymers by high-resolution atomic force microscopy. *Chem. Soc. Rev.* **38**, 737 (2009).
- Liu, Y. & Vancso, G. J. Polymer single chain imaging, molecular forces, and nanoscale processes by Atomic Force Microscopy: The ultimate proof of the macromolecular hypothesis. *Prog. Polym. Sci.* **104** <https://doi.org/10.1016/j.progpolymsci.2020.101232> (2020).
- Kurouski, D., Deckert-Gaudig, T., Deckert, V. & Lednev, I. K. Structure and composition of Insulin Fibril surfaces probed by TERS. *J. Am. Chem. Soc.* **134**, 13323–13329 (2012).
- Lee, J., Crampton, K. T., Tallarida, N. & Apkarian, V. A. Visualizing vibrational normal modes of a single molecule with atomically confined light. *Nature* **568**, 78–82 (2019).
- Shao, F. et al. In-situ nanospectroscopic imaging of plasmon-induced two-dimensional [4 + 4]-cycloaddition polymerization on Au(111). *Nat. Commun.* **12**, 4557 (2021).
- Mrđenović, D. et al. Visualizing surface phase separation in PS-PMMA polymer blends at the nanoscale. *ACS Appl. Mater. Interfaces* **14**, 24938–24945 (2022).
- Mrđenović, D. et al. Nanoscale chemical analysis of 2D molecular materials using tip-enhanced Raman spectroscopy. *Nanoscale* **15**, 963–974 (2023).
- Centrone, A. Infrared Imaging and Spectroscopy Beyond the Diffraction Limit. *Annu. Rev. Anal. Chem.* **8**, 101–126 (2015).
- Kurouski, D., Dazzi, A., Zenobi, R. & Centrone, A. Infrared and Raman chemical imaging and spectroscopy at the nanoscale. *Chem. Soc. Rev.* **49**, 3315–3347 (2020).
- Ruggeri, F. S., Mannini, B., Schmid, R., Vendruscolo, M. & Knowles, T. P. J. Single molecule secondary structure determination of proteins through infrared absorption nanospectroscopy. *Nat. Commun.* **11**, 2945 (2020).
- Jin, M. & Belkin, M. A. Infrared Vibrational Spectroscopy of functionalized atomic force microscope probes using resonantly enhanced infrared Photoexpansion Nanospectroscopy. *Small Methods* **3**, 1900018 (2019).
- Tseng, Y.-H. et al. Photoinduced Alignment under Solvent Vapor Annealing (PA-SVA): Enhanced ordering and patterning in block copolymer films. *ACS Appl. Polym. Mater.* **4**, 8536–8542 (2022).
- Prine, N. et al. Enabling quantitative analysis of complex polymer blends by infrared nanospectroscopy and isotopic deuteration. *Nanoscale* **15**, 7365–7373 (2023).
- Liang, D.-D., Pujari, S. P., Subramaniam, M., Besten, M. & Zuillhof, H. Configurationally Chiral SuFEx-Based Polymers. *Angew. Chem. Int. Ed.* **61**, e202116158 (2022).
- Li, S. et al. SuFExable polymers with helical structures derived from thionyl tetrafluoride. *Nat. Chem.* **13**, 858–867 (2021).
- Ruggeri, F. S. et al. Nanoscale studies link amyloid maturity with polyglutamine diseases onset. *Sci. Rep.* **6**, 31155 (2016).
- Korolkov, V. V. et al. Ultra-high resolution imaging of thin films and single strands of polythiophene using atomic force microscopy. *Nat. Commun.* **10**, 1537 (2019).
- Shen, J. & Okamoto, Y. Efficient separation of Enantiomers using stereoregular chiral polymers. *Chem. Rev.* **116**, 1094–1138 (2016).
- Ranjbar, B. & Gill, P. Circular dichroism techniques: biomolecular and nanostructural analyses- a review. *Chem. Biol. Drug Des.* **74**, 101–120 (2009).
- Bulheller, B. M., Rodger, A. & Hirst, J. D. Circular and linear dichroism of proteins. *Phys. Chem. Chem. Phys.* **9**, 2020–2035 (2007).

42. Kane-Maguire, L. A. P. & Wallace, G. G. Chiral conducting polymers. *Chem. Soc. Rev.* **39**, 2545–2576 (2010).
43. Nakano, T., Pietropaolo, A. & Kamata, M. Chirality analysis of helical polymers. *Chem. Teach. Int.* **3**, 131–140 (2021).
44. Nakano, T. & Okamoto, Y. Synthetic helical polymers: Conformation and function. *Chem. Rev.* **101**, 4013–4038 (2001).
45. Leigh, T. & Fernandez-Trillo, P. Helical polymers for biological and medical applications. *Nat. Rev. Chem.* **4**, 291–310 (2020).
46. Osman, Z. & Arof, A. K. FTIR studies of chitosan acetate based polymer electrolytes. *Electrochim. Acta* **48**, 993–999 (2003).
47. Wu, L. C. et al. A charge density study of π -delocalization and intermolecular interactions. *Phys. Chem. Chem. Phys.* **17**, 14177–14184 (2015).
48. Dharmawardana, M. et al. Strong π -stacking causes unusually large anisotropic thermal expansion and thermochromism. *PNAS* **118**, e2106572118 (2021).
49. Kenkel, S., Mittal, S. & Bhargava, R. Closed-loop atomic force microscopy-infrared spectroscopic imaging for nanoscale molecular characterization. *Nat. Commun.* **11**, 3225 (2020).
50. Marinello, F., Balcon, M., Carmignato, S. & Savio, E. Long term thermal drift study on SPM scanners. *Mechatronics* **21**, 1272–1278 (2011).
51. Hirata, S., Shigeta, Y., Xantheas, S. S. & Bartlett, R. J. Helical organic and inorganic polymers. *J. Phys. Chem. B* **127**, 3556–3583 (2023).
52. Rohmer, M., Freudenberg, J. & Binder, W. H. Secondary Structures in Synthetic Poly(Amino Acids): Homo- and Copolymers of Poly(Aib), Poly(Glu), and Poly(Asp). *Macromol. Biosci.* **23**, 2200344 (2023).
53. Watson, J. L. et al. De novo design of protein structure and function with RFdiffusion. *Nature* **620**, 1089–1100 (2023).
54. Liang, D.-D. et al. Silicon-Free SuFEx reactions of sulfonimidoyl fluorides: scope, enantioselectivity, and mechanism. *Angew. Chem. Int. Ed.* **59**, 7494–7500 (2020).

Acknowledgements

FSR has received funding from the Dutch Sector Plan beta. The authors thank the support and funding of the Shared Research Facilities (SRF) of Wageningen University and Research (The Netherlands). The authors gratefully acknowledge the facility NanoFACT (Wageningen, The Netherlands) for the support and assistance in undertaking this work.

Author contributions

F.S.R. and X.L. conceived the project. X.L. performed the CD, IR, and AFM experiments, F.S.R. and X.L. analysed the relative data. F.S.R. and X.L. performed the AFM-IR experiments and analysed the relative data. S.P. synthesised the molecules and the polymers, performed the HPLC,

NMR, GPC, MS experiments and analysed the relative data. X.L. and F.S.R. wrote the original draft of the manuscript. F.S.R., J.V.G., H.Z. supervised X.L. H.Z. supervised S.P. All the authors revised and commented the manuscript.

Competing interests

The authors declare no competing interests.

Additional information

Supplementary information The online version contains supplementary material available at <https://doi.org/10.1038/s41467-025-62041-0>.

Correspondence and requests for materials should be addressed to Han Zuilhof or Francesco Simone Ruggeri.

Peer review information *Nature Communications* thanks Chun-Sen Liu, Kalathil Krishnan Kartha, and the other, anonymous, reviewer(s) for their contribution to the peer review of this work. A peer review file is available.

Reprints and permissions information is available at <http://www.nature.com/reprints>

Publisher's note Springer Nature remains neutral with regard to jurisdictional claims in published maps and institutional affiliations.

Open Access This article is licensed under a Creative Commons Attribution-NonCommercial-NoDerivatives 4.0 International License, which permits any non-commercial use, sharing, distribution and reproduction in any medium or format, as long as you give appropriate credit to the original author(s) and the source, provide a link to the Creative Commons licence, and indicate if you modified the licensed material. You do not have permission under this licence to share adapted material derived from this article or parts of it. The images or other third party material in this article are included in the article's Creative Commons licence, unless indicated otherwise in a credit line to the material. If material is not included in the article's Creative Commons licence and your intended use is not permitted by statutory regulation or exceeds the permitted use, you will need to obtain permission directly from the copyright holder. To view a copy of this licence, visit <http://creativecommons.org/licenses/by-nc-nd/4.0/>.

© The Author(s) 2025